Supplementary Information

Amorphous Indium-zinc Oxide Layer with Transport and Protective Dual-Function for High-Efficiency Semitransparent and Tandem $Sb_2(S,Se)_3$ Solar Cells

Junjie Yang[a], Jianyu Li[a], Yuehao Gu[a], Rongfeng Tang[*a], Lei Huang[a], Zhiyuan Cai[a], Bo Che[a], Qi Zhao[a], Shuwei Sheng[a], Hong Wang[b], Changfei Zhu[a], Tao Chen[*a]

a J. Yang, J. Li, Y. Gu, R. Tang, L Huang, Z. Cai, B. Che, Q. Zhao, S. Sheng, C. Zhu, T. Chen
Hefei National Research Center for Physical Sciences at the Microscale, School of Chemistry and Materials Science, Key Laboratory of Energy Conversion Materials, Chinese Academy of Sciences, University of Science and Technology of China, Hefei, Anhui 230026, P. R. China.
E-mail: rftang@ustc.edu.cn, tchenmse@ustc.edu.cn.

b H. Wang
Department of Environmental Science and Engineering, University of Science and Technology of China, Hefei 230026, P. R. China.

*Corresponding Author: rftang@ustc.edu.cn (R. Tang), tchenmse@ustc.edu.cn (T. Chen).

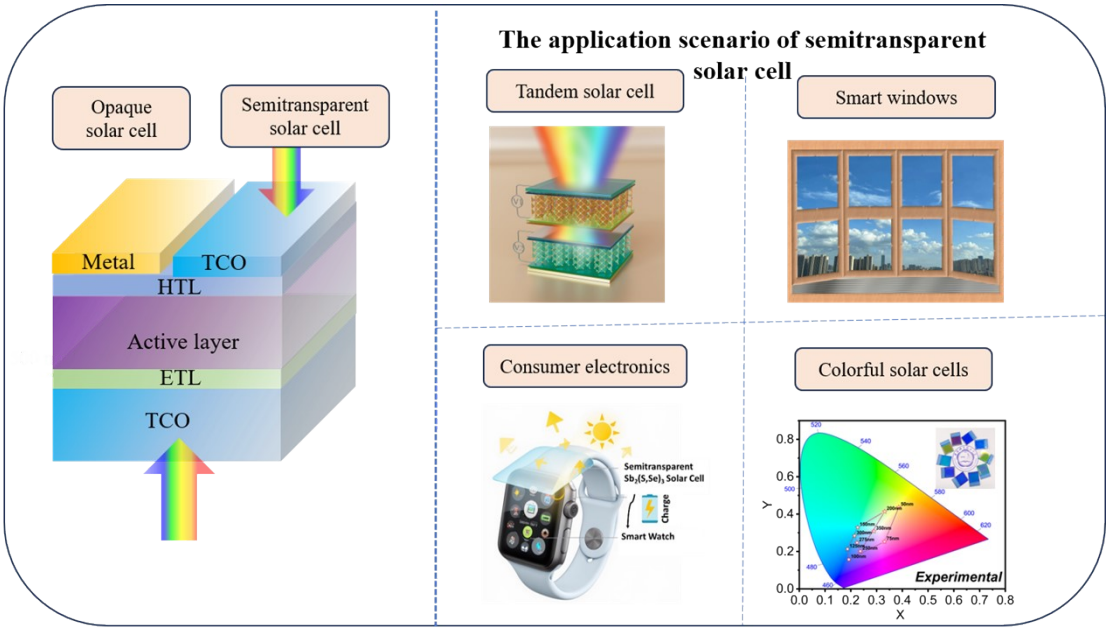

Fig. S1 The schematic of the difference between semitransparent solar cells and opaque solar cells (left), the advantages and special application scenarios of semitransparent solar cells (right).

Note S1 The Definition and Comparison of Soft-Sputtering

Through investigating how varying sputtering power densities influence IZO film properties, their impact on MnS and the performance of semitransparent $Sb_2(S,Se)_3$ solar cells, we systematically elucidated the interplay between sputtering power density, IZO film characteristics, and MnS integrity, ultimately correlating these factors with the performance optimization of semitransparent $Sb_2(S,Se)_3$ solar cells through conductivity-damage trade-off analysis.

Structural, optical and morphological properties of IZO films.

First, we studied the differences in the structural, optical and morphological properties of IZO sputtered at different power densities. The results of XRD show that IZO films sputtered at different power densities all maintain amorphous properties (Fig. S2a). From the UV-vis results of IZO (Fig. S2b and 2c, and table S1), we found that the average transmittance of IZO films sputtered at low power density in the range of 400-1200 nm is slightly higher than that of films sputtered at 3.54 W/cm^2. On the other hand, the bandgap of the two films are relatively close, both about 3.75 eV. In addition, the surface morphology of IZO thin films is also minimally affected by sputtering power density, as shown in the results of SEM. Therefore, the power density has little effect on the structural, optical and morphological properties of the sputtered IZO films.

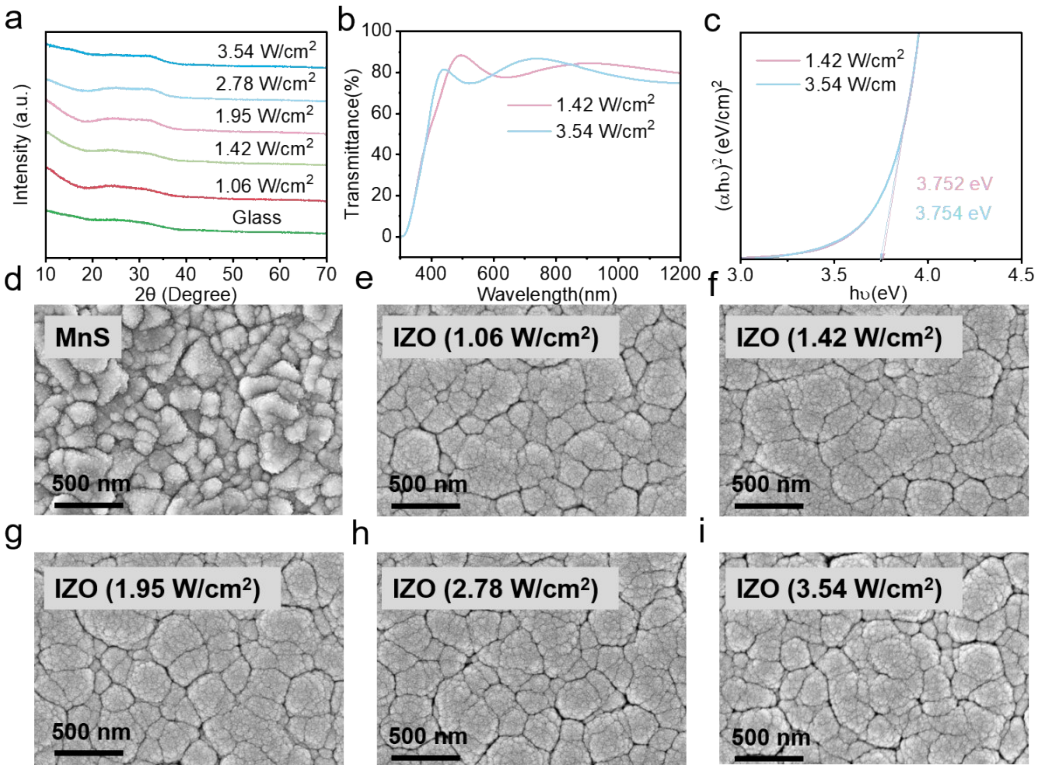

Fig. S2 The structural, optical and morphological properties of IZO films. (a) XRD patterns for the glass and IZO films sputtered at power densities of 1.06, 1.42, 1.95, 2.78, 3.54 W/cm^2. (b, c) The optical transmittance and bandgap of IZO films sputtered at 1.42 and 3.54 W/cm^2. (d-i) surface morphology the MnS and IZO films sputtered at power densities of 1.06, 1.42, 1.95, 2.78, 3.54 W/cm^2.

Electrical properties of IZO films.

Fig. S3a-d show the electrical properties of IZO film sputtered at different sputtering power density. As shown in Fig. S3a, the mobility of IZO film reaches the maximum of 24.41 cm^2/(V·s) when power density increasing from 1.06 to 1.95 W/cm^2. When the sputtering power is further increased, the carrier mobility gradually decreases. Carrier concentration increases with sputtering power density increasing continuously, in agreement with the results in the literature[1]. The carrier concentration of the IZO film sputtered at low power density (1.06 W/cm^2) is only 2.1x10^{19} cm^{-3}. When the sputtering power density is increased to 3.54 W/cm^2, the carrier concentration is as high as 5.99x10^{20} cm^{-3}. Therefore, the resistivity and square resistance decrease with the increase of sputtering power density, and reaches the minimum value of 1.2x10^{-3}Ω·cm and 21.9 Ω·sq^{-1} at 3.54 W/cm^2, as shown in Fig. S3c and 3d. It is noteworthy that the conductivity of the sputtered IZO film is still poor when the power density is 1.06 W/cm^2, but the square resistance of the IZO film significantly decreases from 255 Ω·sq^{-1} to 60.9 Ω·sq^{-1} when the power density is increased to 1.42 W/cm^2.

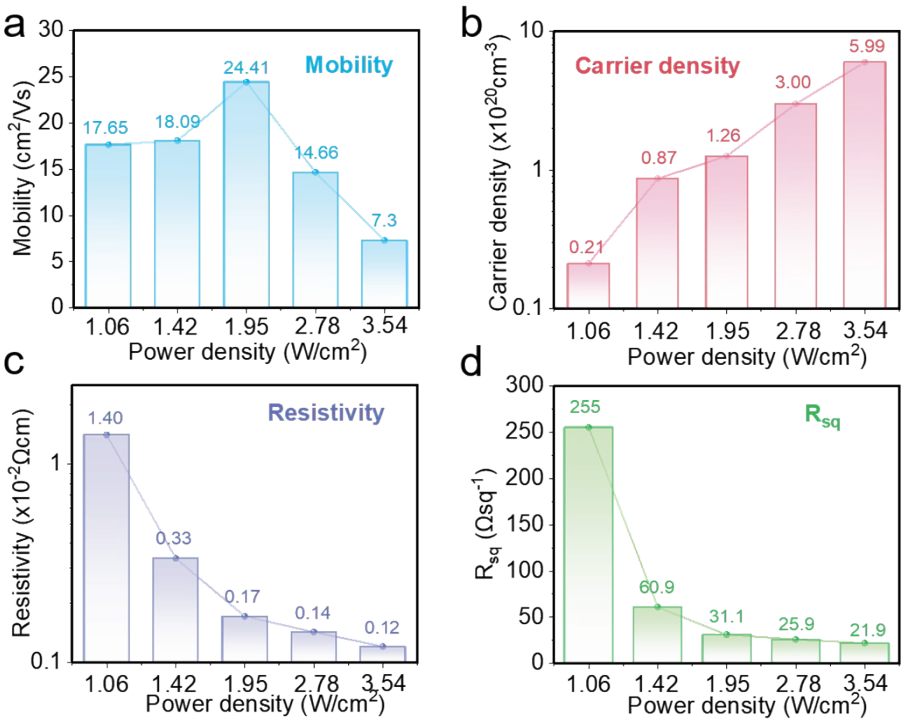

Fig. S3 Electrical properties of IZO films. (a) Mobility, (b) carrier concentration, (c) resistivity and (d) square resistance (R_{sq}) of IZO films sputtered at power densities of 1.06, 1.42, 1.95, 2.78, 3.54 W/cm^2.

Effect of IZO sputtered at different power densities on MnS

We employed the EDS technique to investigate the impact of IZO sputtered at varying power densities on the elemental composition of MnS. To circumvent test errors, we examined the elemental content at 10 distinct locations of each sample. As demonstrated in Fig. S4a and S4b, the sulfur content in MnS experiences a gradual decrease with increasing sputtering power, while the manganese content increases. Consequently, the S/Mn ratio undergoes a gradual decrease with rising sputtering power density. The sulfur content of MnS in the absence of IZO sputtering is 48.39%. When IZO is sputtered at low power density, the damage to MnS is minimal, with the sulfur content of MnS dropping to 48.24% (1.06 W/cm^2) and 48.02% (1.42W/cm^2). However, when the sputtering power is augmented to 2.78 and 3.54 W/cm^2, the sulfur content experiences a decline to 46.90% and 46.51%, respectively. The EDS energy spectrum also show a gradual decrease in the S/Mn signal with increasing sputtering power (Fig. S4e). Therefore, the preparation of IZO film by magnetron sputtering causes certain damage to the MnS layer, resulting in a reduction in anions. It is evident

that the greater the sputtering power density, the more severe the damage and the greater the loss of sulfur element.

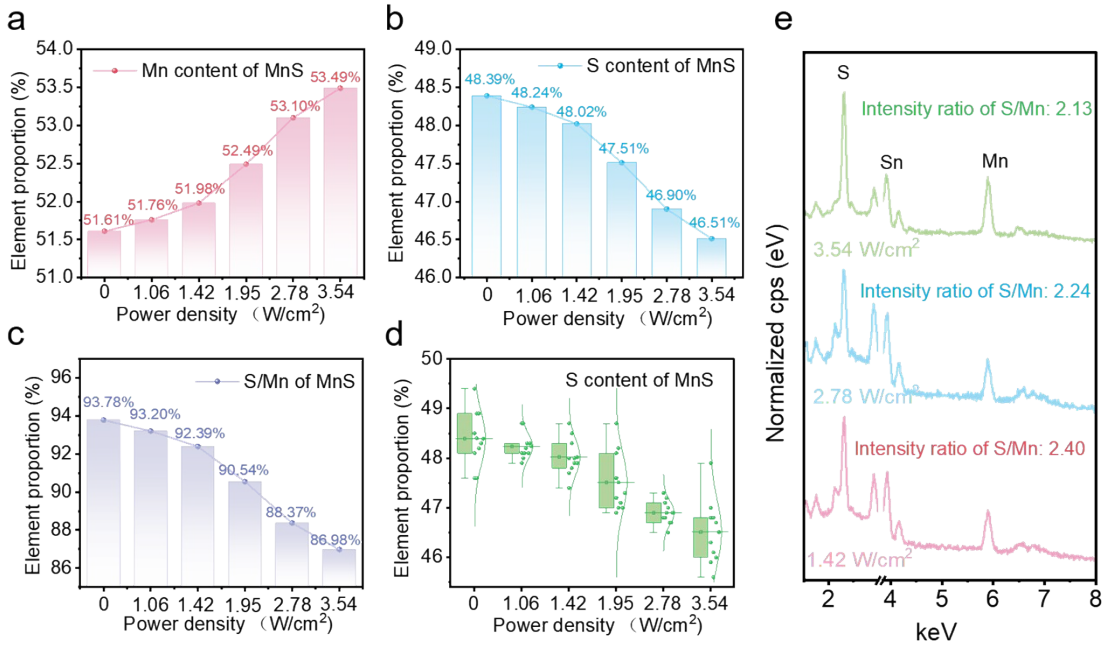

Fig. S4 Effect of IZO sputtered at different power densities on elemental composition of MnS. (a) Mn content, (b) S content, (c) S/Mn and (d) statistics of S content of MnS. (e) the EDS spectrum of MnS.

Effect of IZO sputtered at different power densities on device performance

Finally, we explored the impact of IZO sputtered at different power densities on the performance of semitransparent $Sb_2(S,Se)_3$ solar cells, as illustrated in Fig. S5. Our findings reveal that the absence of IZO results in the poorest device performance, attributable to the presence of a contact barrier between MnS and ITO, as well as the damage to MnS caused by sputtering ITO. However, the incorporation of IZO into the device led to a notable enhancement in the performance. Specifically, when the sputtering power density of IZO is increased from 1.06 W/cm^2 to 1.42 W/cm^2, the optimal performance of the device is increased from 7.71% to 8.26%, which may be attributed to the significant increase in conductivity of the IZO film and the avoidance of excessive sulfur loss. However, when the sputtering power density is further increased, the photovoltaic performance of the device undergoes a gradual decline, primarily due to the incremental increase in sputtering damage. Consequently, the

conductivity of the IZO film and the sputtering damage exhibit a contradictory relationship. In summary, insufficient sputtering power density can lead to high resistivity of TCO, while high power density can cause serious sputtering damage, both of which are detrimental to the improvement of device performance. Therefore, the trade-off between conductivity enhancement and suppression of sputter damage defines the "soft-sputtering" window. In our research results, 1.42 W/cm^2 is determined as the critical threshold, at which the device performance is optimized by maximizing conductivity and minimizing sputtering damage.

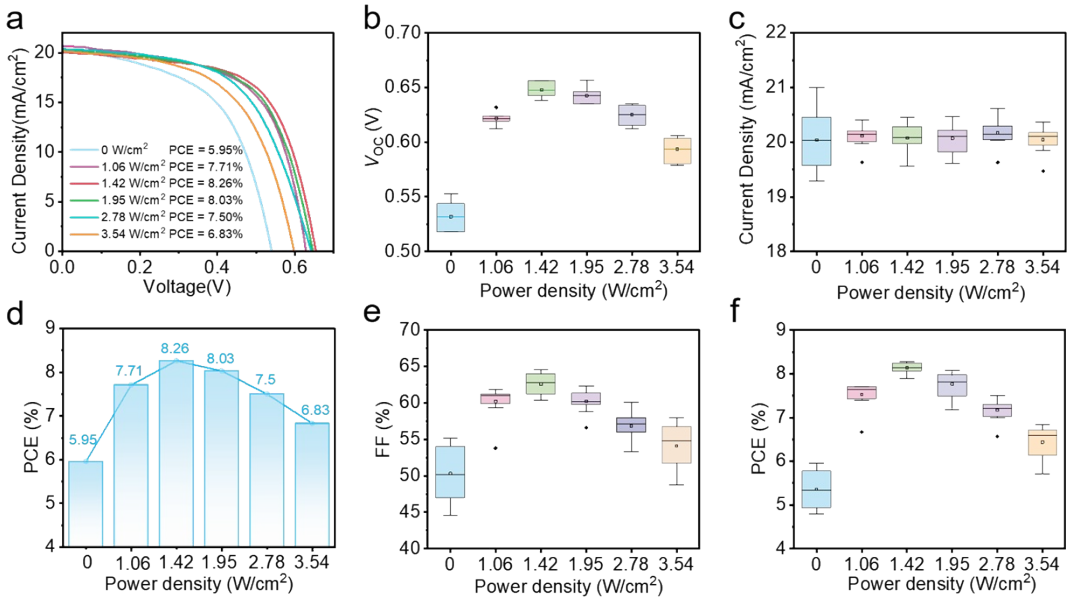

Fig. S5 Effect of IZO sputtered at different power densities on device performance. (a) J-V curves of the semitransparent devices. (b, c, e, f) Statistics of the VOC, FF, JSC, and PCE of the devices. (d) the optimal performance of the devices based on different power densities.

Note S2 The Clarification for the discrepancy of the EQE curves

The Semi-IZO configuration shows a notably lower response in the long-wavelength region compared to the Semi-Control configuration, while it exhibits enhanced external quantum efficiency in the short-wavelength region. Consequently, the overall integrated current densities between the two devices are very similar.

Our devices employ CdS as the electron transport layer in the $Sb_2(S,Se)_3$ solar cell, which is a commonly used and highly effective material with a bandgap of approximately 2.4 eV. Due to its relatively narrow bandgap, CdS can incur significant parasitic absorption, particularly in the 400-550 nm range, which typically results in a dip in the EQE spectrum.[1] The thickness of the CdS layer plays an important role: a thicker CdS enhances carrier extraction but also increases parasitic absorption, while a thinner CdS minimizes absorption losses but may compromise charge extraction efficiency. This trade-off is inherent in this planar heterojunction solar cells.[2]

We suspect that the differences observed in the long and short-wavelength responses between the Semi-IZO and Semi-Control devices arise from variations in the CdS film thickness, which is deposited via chemical bath deposition (CBD). The CBD process is highly sensitive to environmental factors such as temperature, humidity, and pH variations (due to ammonia evaporation), leading to differences in CdS thickness even under otherwise identical conditions.

To investigate this further, we prepared CdS films with various growth times (14 min 30 s, 15 min 30 s, 16 min, and 17 min) on the same day to simulate the effects of environmental variations on CdS thickness. We then fabricated semitransparent $Sb_2(S,Se)_3$ solar cells with these CdS films and measured their photovoltaic performance and EQE responses. As shown in Fig. S6a, the EQE spectral response systematically changes with CdS thickness: thinner CdS layers exhibit less parasitic absorption in the short-wavelength region but poorer response in the long-wavelength region. Interestingly, the integrated current density of the devices remains almost constant, confirming the trade-off between parasitic absorption and efficient carrier extraction.

Further comparisons of Semi-IZO and Semi-Control devices under every different CdS thicknesses (Fig. S6b, c, e, f) indicate that the spectral response curves are very similar, and the integral current density undergoes negligible alterations. This strongly

suggests that the primary performance enhancements in Semi-IZO devices are due to improvements in Voc and FF, while the current density remains nearly identical.

This explanation clarifies the underlying causes of the observed EQE differences and demonstrates that the variations are mainly attributable to the inherent trade-off between parasitic absorption and carrier extraction caused by variations in CdS thickness.

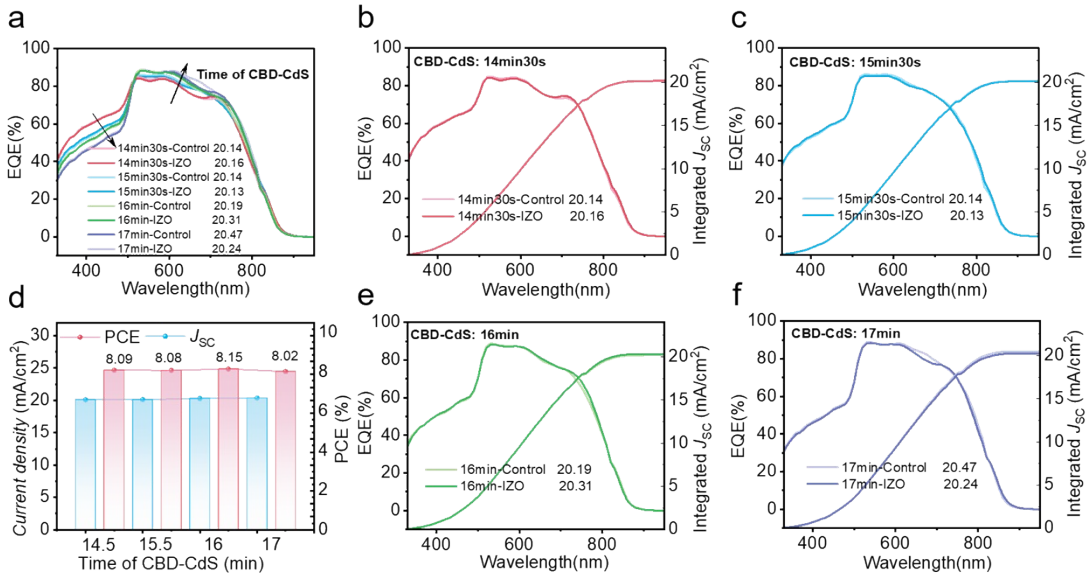

Fig. S6 Effect of deposition durations of CBD-CdS on Photoelectrical properties of the semitransparent devices. (a) EQE spectra of the Semi-Control and Semi-IZO devices based on different deposition durations of CdS film. (b, c, e, f) EQE spectra and the corresponding integrated current density of the Semi-Control and Semi-IZO devices based on CdS film prepared with a duration of 14min 30s, 15min 30s, 16min and 17min. (d) PCE and J_{SC} of the corresponding Semi-IZO devices.

The EQE of opaque devices bears a resemblance to the EQE spectral response of the semi-transparent device. The discrepancy can be attributed to the minor discrepancy in the thickness of the CDS of the respective champion efficiency devices. This discrepancy leads to a trade-off in parasitic absorption and carrier extraction, which exhibits different advantages in different devices. To confirm this, we fabricated both Opa-control and Opa-IZO devices with CdS layers of identical thickness and measured their EQE responses. As shown in Fig. S7, the spectral responses and integrated short-circuit current densities of these devices are nearly identical, consistent with the J_{SC} measured by J-V carve.

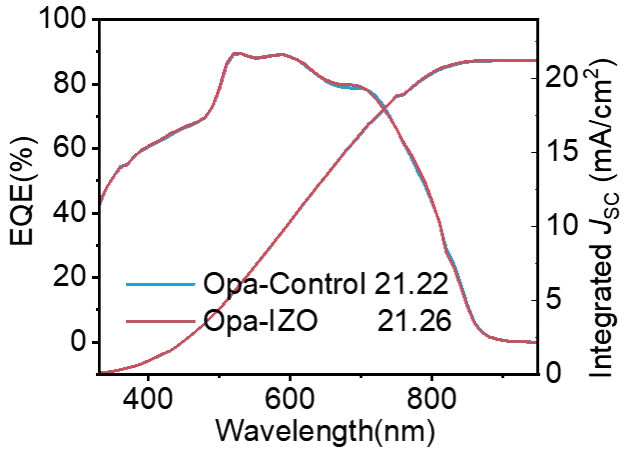

Fig. S7 EQE spectra of the Opa-Control and Opa-IZO devices based on same time of CBD-CdS.

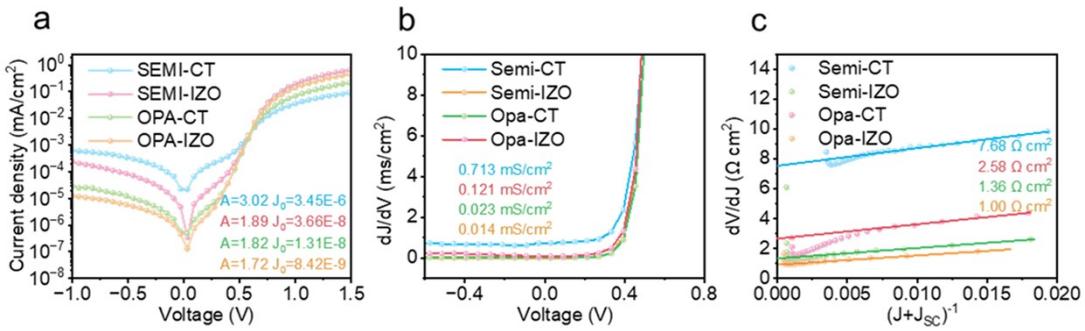

Fig. S8 Electrical behaviors of the control- and IZO-based semitransparent and opaque $Sb_2(S,Se)_3$ solar cells. a) Dark J-V curves for ideality factor A and reverse saturation current density J_0, b) shunt conductance G characterizations, c) series resistance R characterizations.

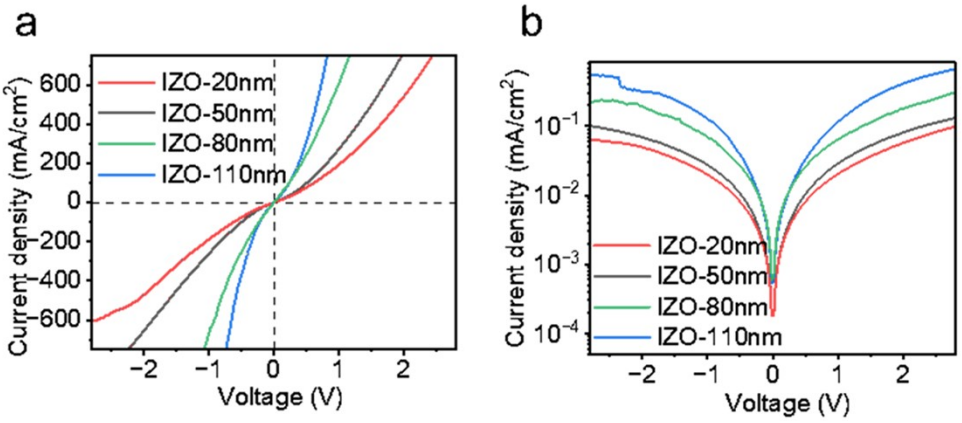

Fig. S9 a) *J-V* characteristics of the hole-only devices (FTO/NiO_x/MnS/IZO) with different thickness of IZO, b) logarithmic plot of *J-V* characteristic curves.

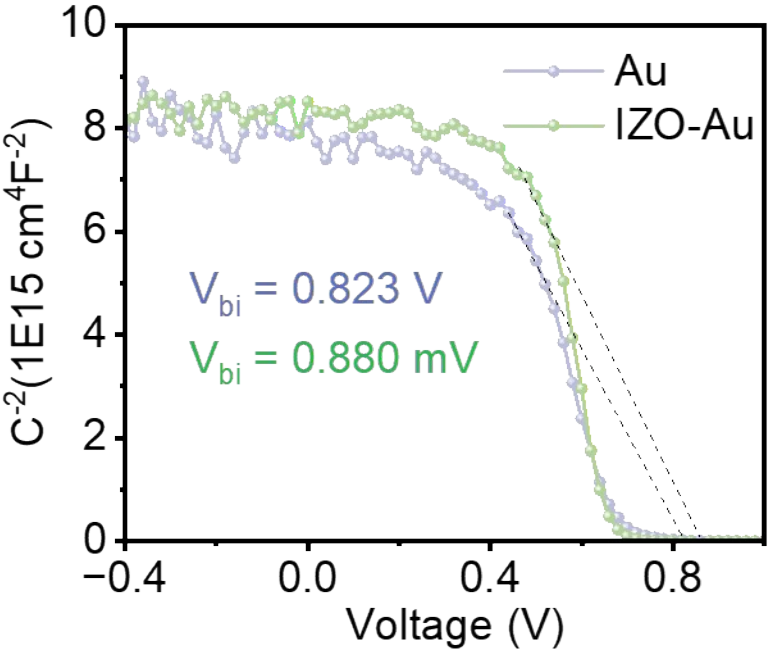

Fig. S10 Mott-Schottky plots of opaque-control- and opaque-IZO-based solar cells.

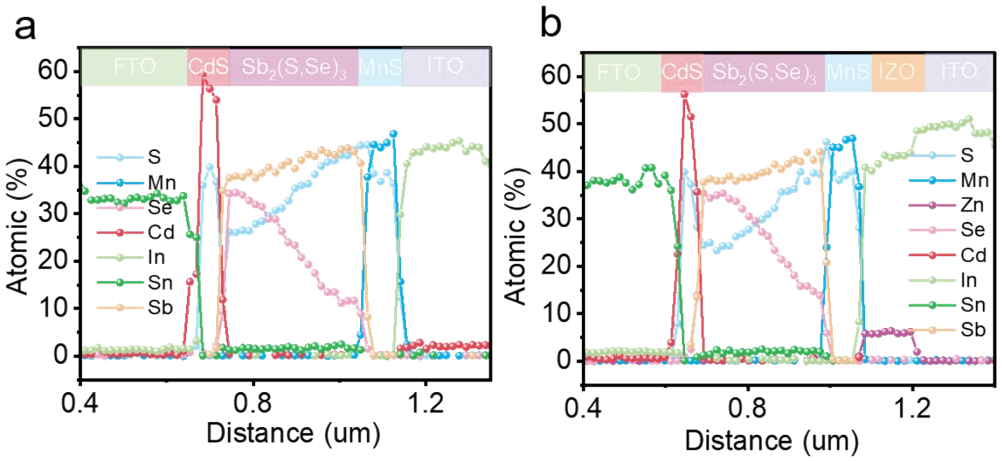

Fig. S11 Retest of TEM-EDS line scan along the depth of the Semi-Control (a) and Semi-IZO (b) devices.

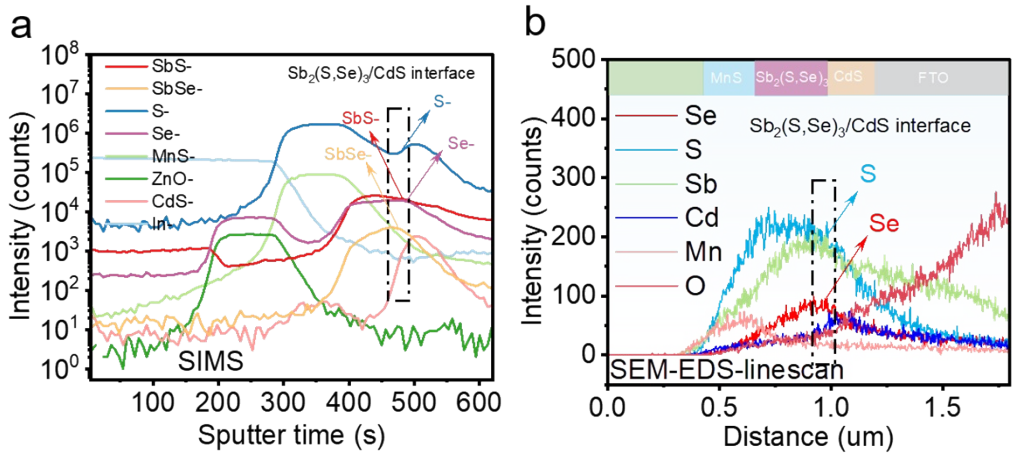

Fig. S12 (a) SIMS profile of the Semitransparent device and (b) SEM-EDS line scan of the device based on FTO/CdS/$Sb_2(S,Se)_3$/MnS.

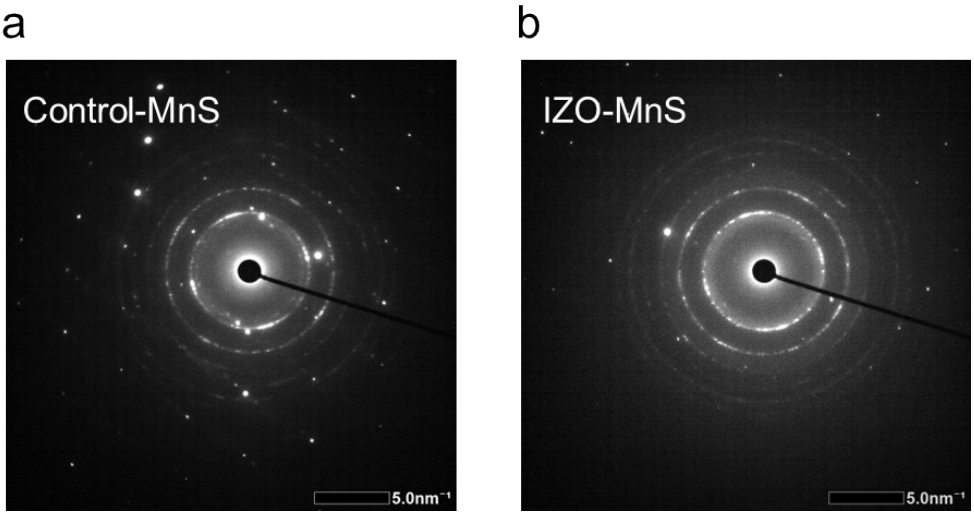

Fig. S13 Selected-area diffraction (SAD) pattern of the Control-MnS and IZO-MnS layers.

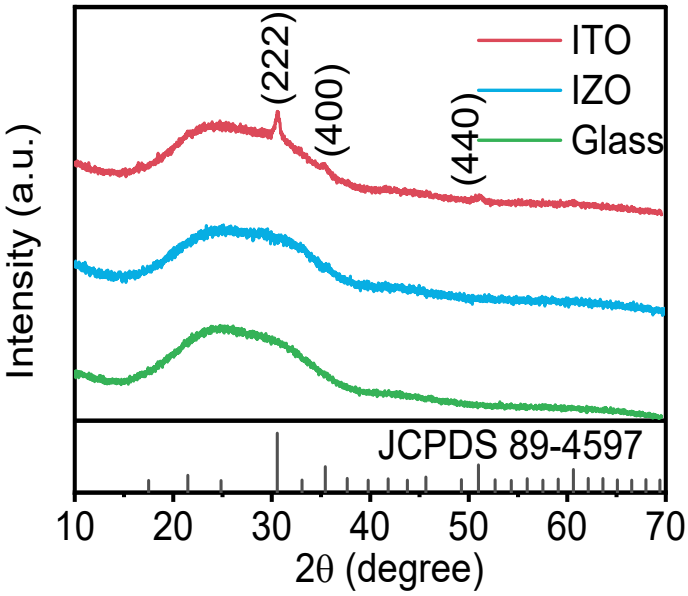

Fig. S14 XRD patterns for the glass, glass/IZO, and glass/ITO samples.

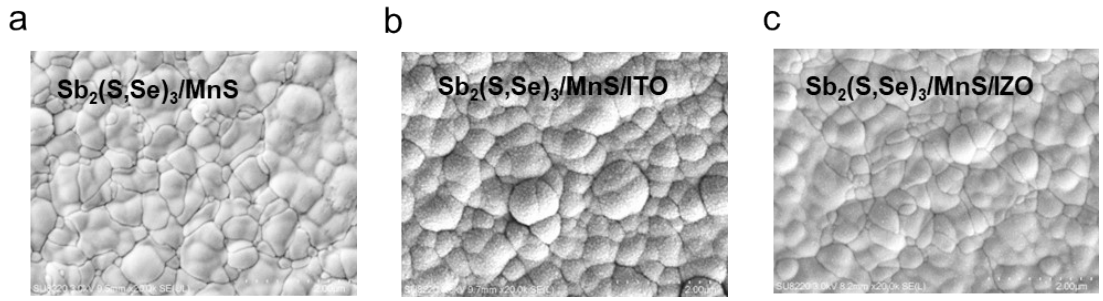

Fig. S15 SEM images of surface morphology for a) FTO/CdS/$Sb_2(S,Se)_3$/MnS, b) FTO/CdS/$Sb_2(S,Se)_3$/MnS/ITO, and c) FTO/CdS/$Sb_2(S,Se)_3$/MnS/IZO.

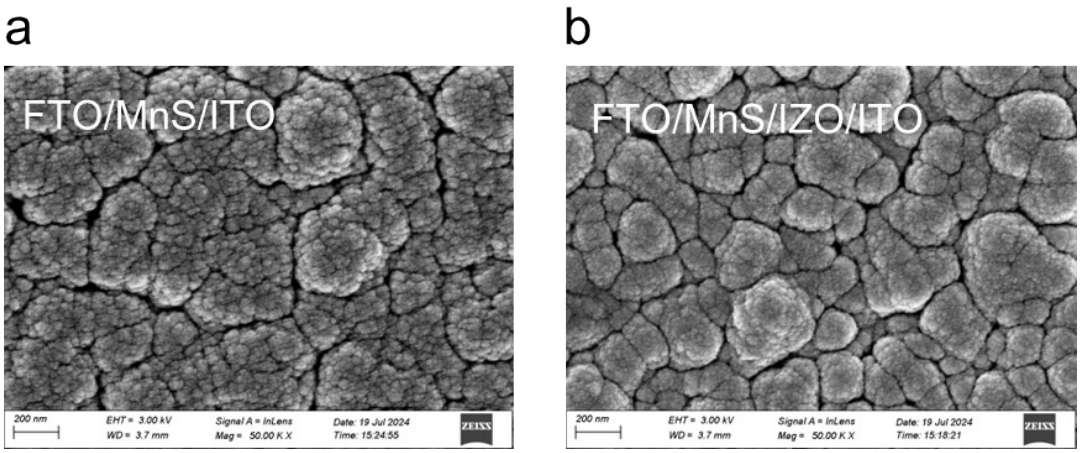

Fig. S16 SEM images of surface morphology for a) FTO/MnS/ITO and b) FTO/MnS/IZO/ITO.

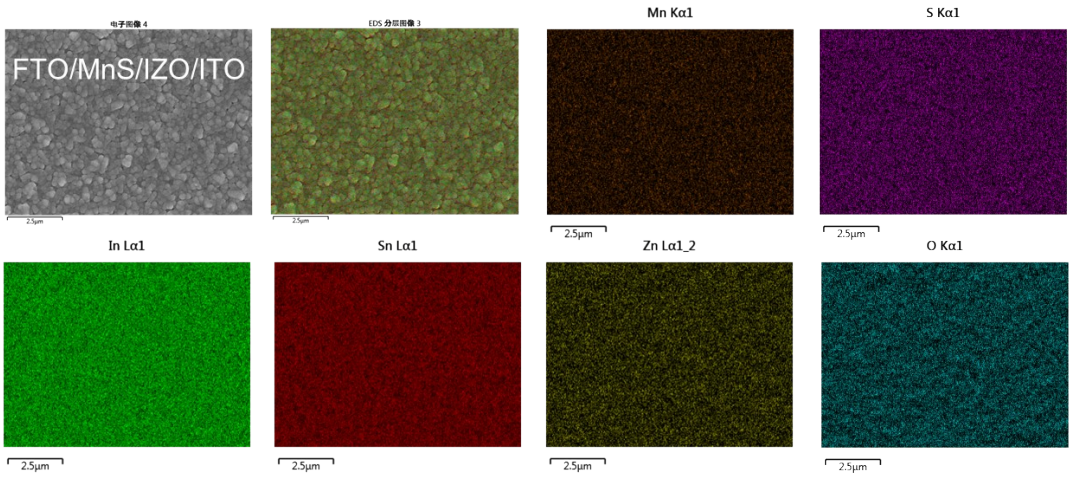

Fig. S17 SEM-EDS mapping on the surfaces of FTO/MnS/IZO/ITO device.

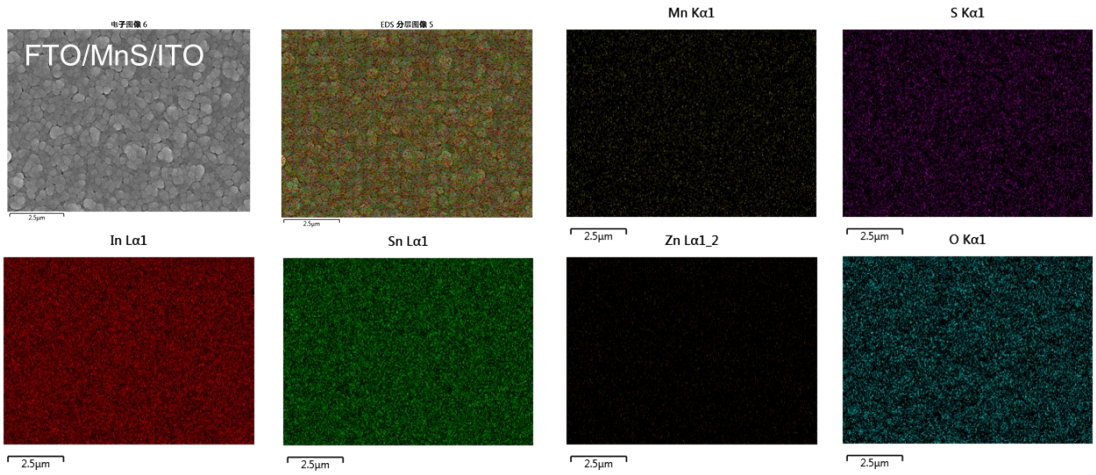

Fig. S18 SEM-EDS mapping on the surfaces of FTO/MnS/ITO device.

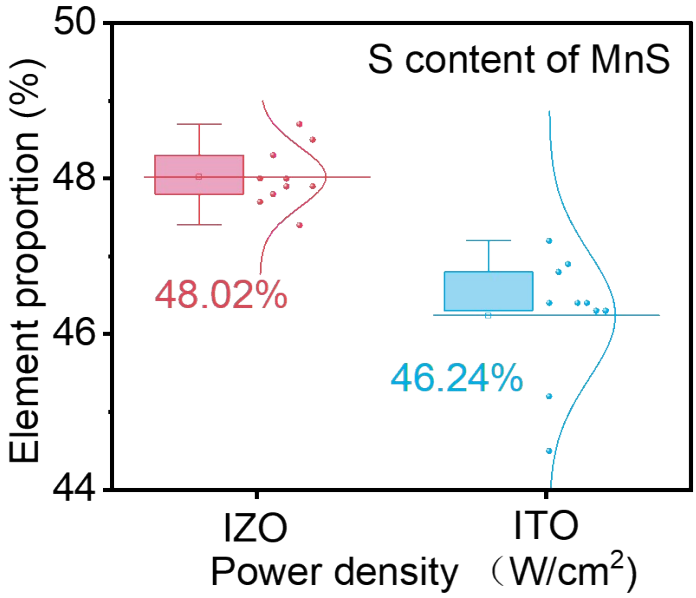

Fig. S19 EDS results of S elemental composition of MnS.

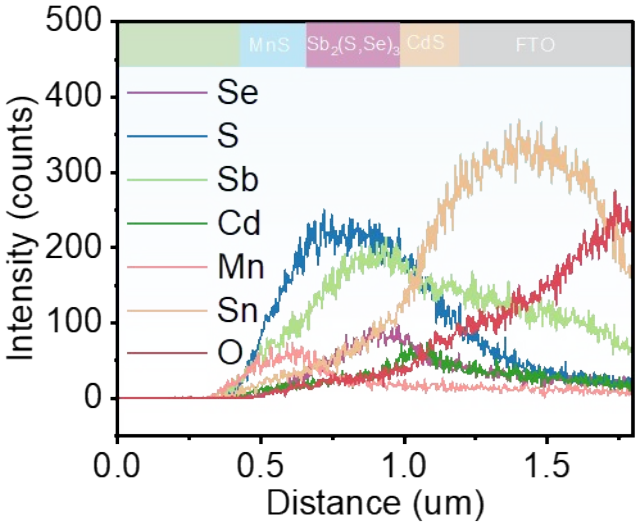

Fig. S20 SEM-EDS line scan of the device based on FTO/CdS/$Sb_2(S,Se)_3$/MnS.

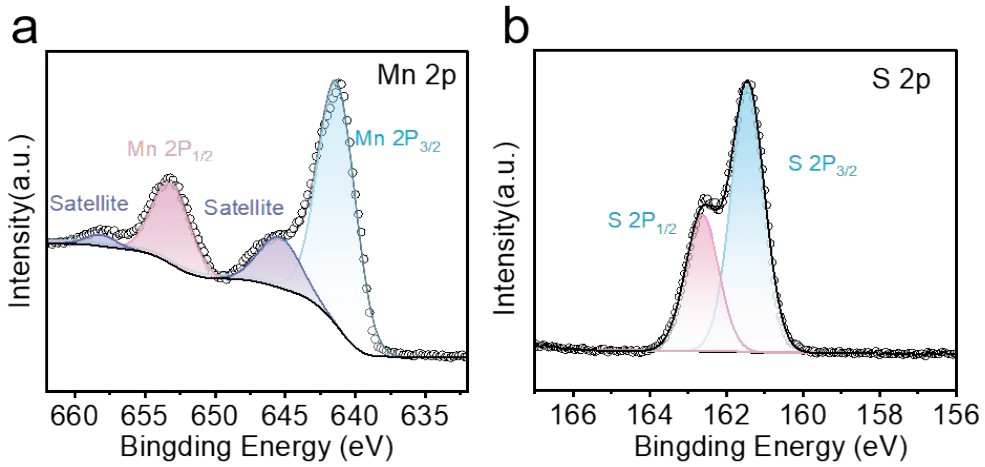

Fig. S21 XPS spectra of (a) Mn 2p and (b) S 2p of MnS thin film.

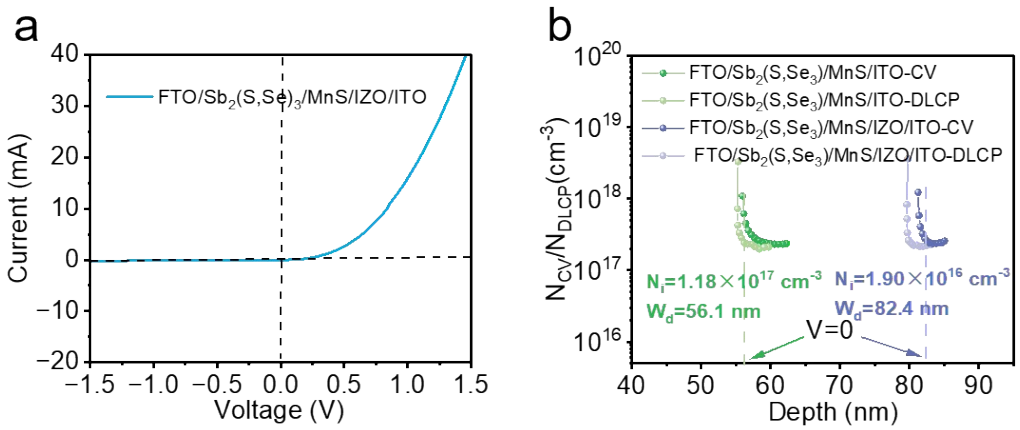

Fig. S22 (a) I-V curves of the FTO/$Sb_2(S,Se)_3$/MnS/IZO/ITO device. (b) C-V and DLCP profiling for the FTO/$Sb_2(S,Se)_3$/MnS/ITO and FTO/$Sb_2(S,Se)_3$/MnS/IZO/ITO devices without CdS electron transport layer.

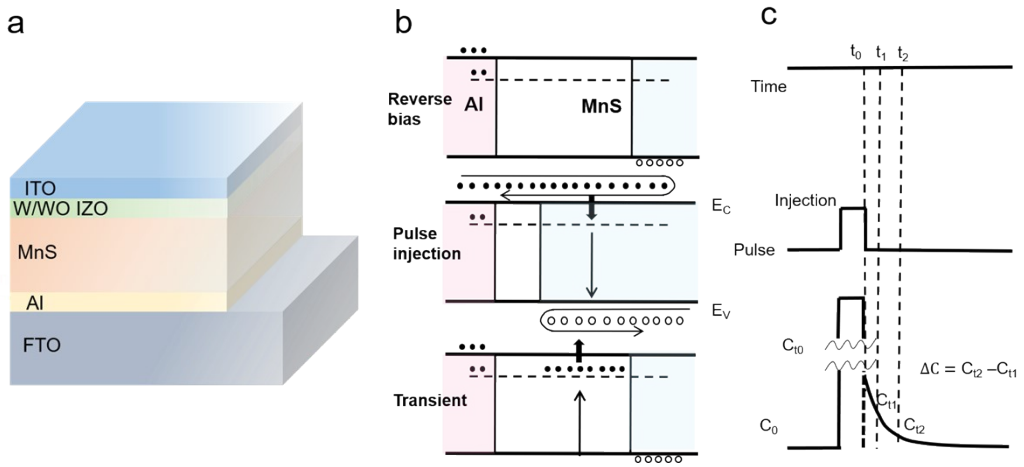

Fig. S23 Schematic diagram of DLTS test. (a) Configuration of the MnS device. (b,c) Schematic illustration of the mechanism for DLTS test using Al and MnS Schottky junction.

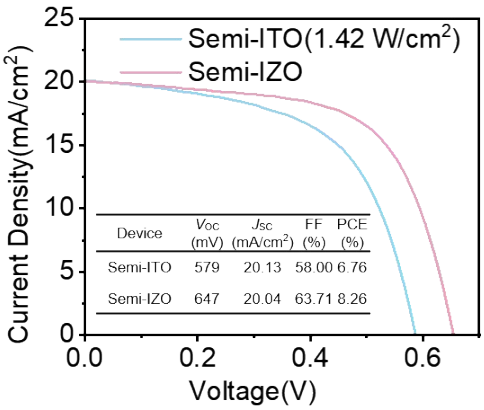

Fig. S24 Photovoltaic performance of the semitransparent $Sb_2(S,Se)_3$ Solar Cells with low power density sputtered ITO and IZO electrodes

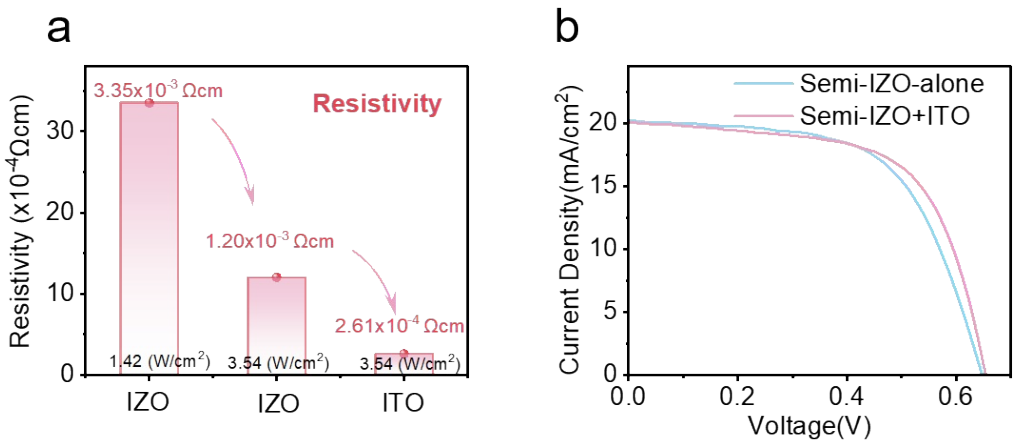

Fig. S25 (a) Resistivity of the IZO and ITO films. (b) Photovoltaic performance of the semitransparent $Sb_2(S,Se)_3$ solar cells with IZO alone and IZO+ITO electrodes.

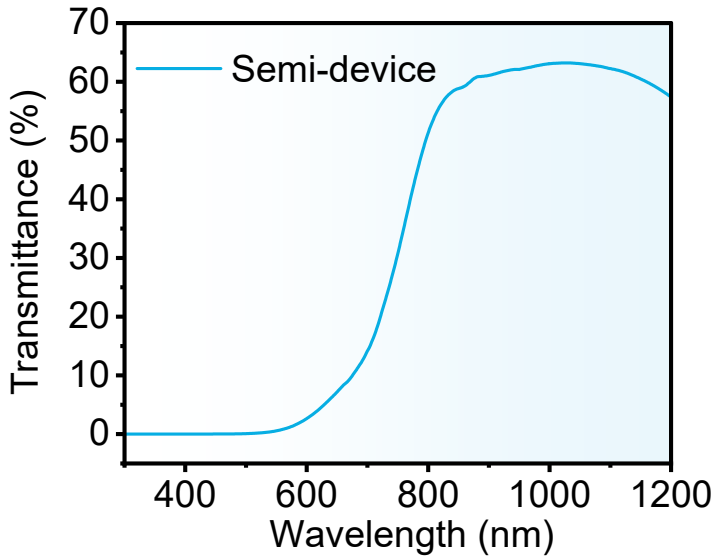

Fig. S26 Transmittance of ST-SSCs devices sputtered with IZO.

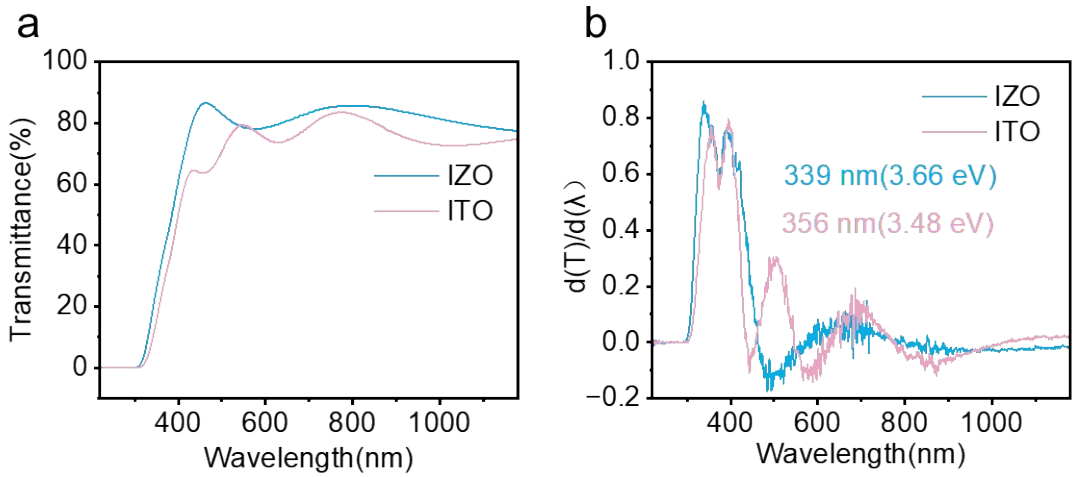

Fig. S27 a) Transmittance of the IZO and ITO. b) The bandgap (Eg) of IZO and ITO.

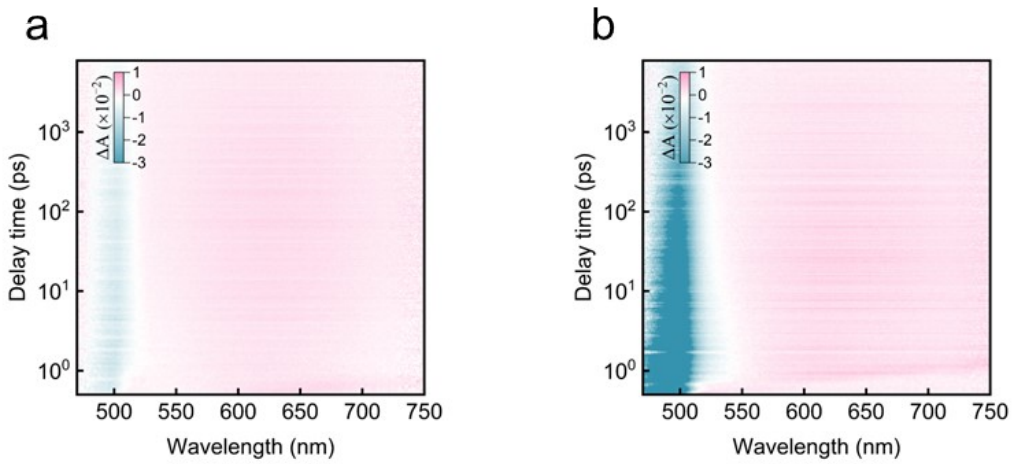

Fig. S28 a, b) 2D color plot of the TA spectra at 450-750 nm for the FTO/CdS/$Sb_2(S,Se)_3$ and the FTO/CdS/$Sb_2(S,Se)_3$/MnS devices incident from the rear side (back side).

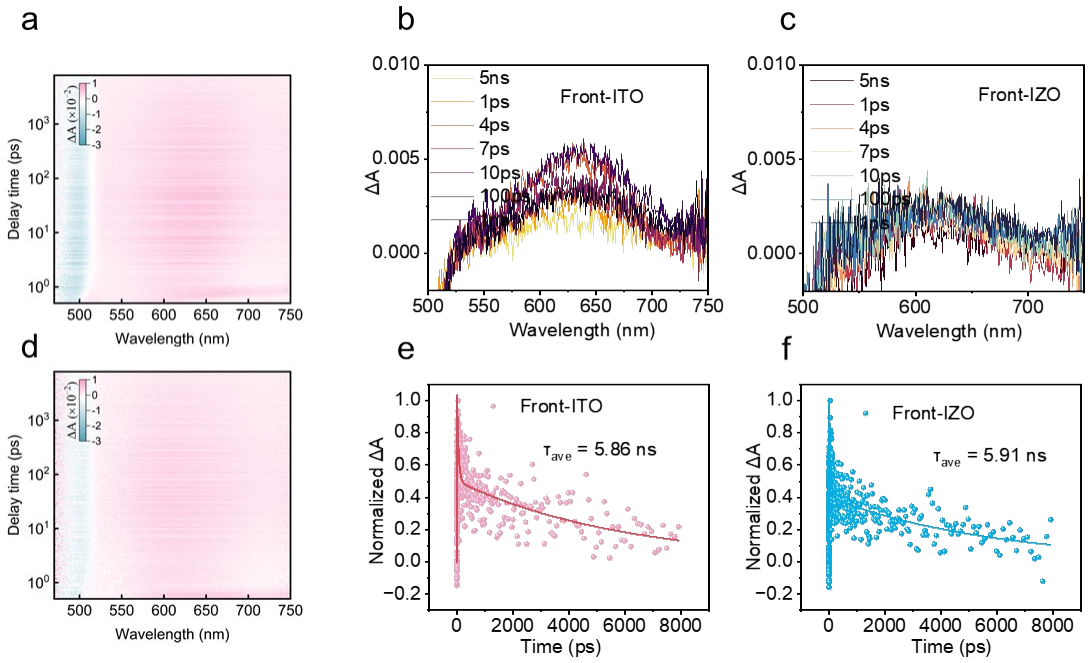

Fig. S29 Transient absorption spectroscopy (TAS) characterization of the ST-SSCs from the Front side. a, d) 2D color plot of the TA spectra at 450-750 nm for the control device and the IZO device incident from the Front side. b, c) Time-resolved absorption spectra obtained at 1 ps - 5 ns from the Front side of the control device and the IZO device. e, f) The normalized dynamics traces probing at 650 nm and the bi-exponential fitting curve of e) the control device and f) the IZO device from the Front side.

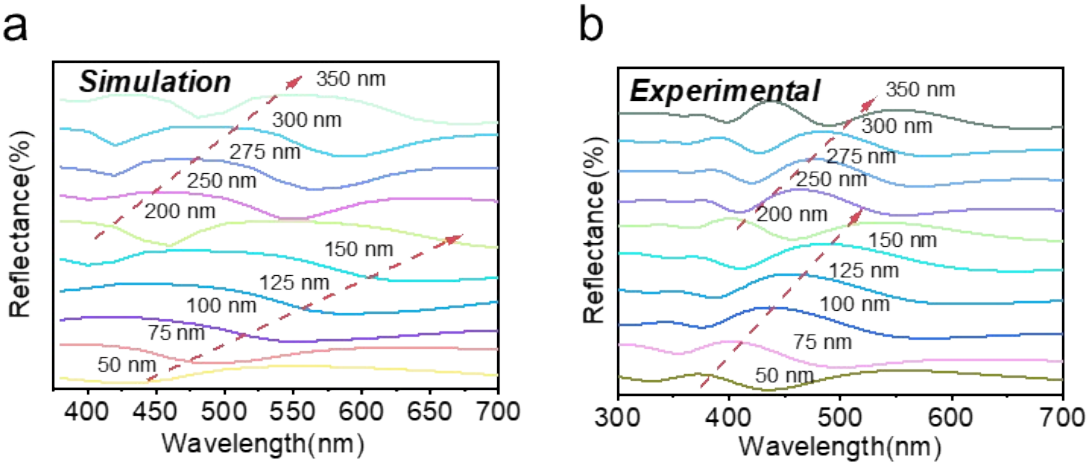

Fig. S30 Simulated and measured reflectance spectra of ST-SSCs with ten different thickness values of ITO

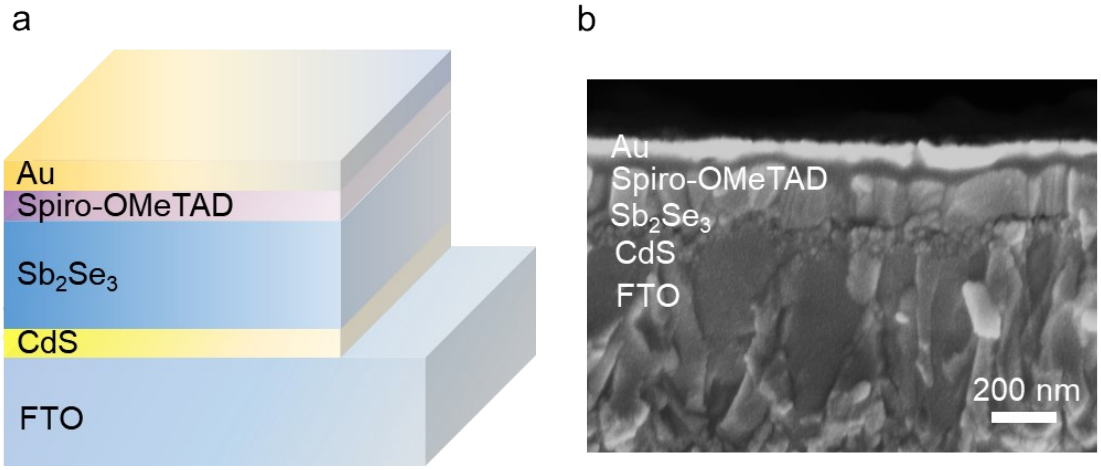

Fig. S31 Device structure of the bottom subcell for 4-T TSCs. a) Device configuration and b) the cross-sectional SEM image of the Sb_2Se_3-based solar cell.

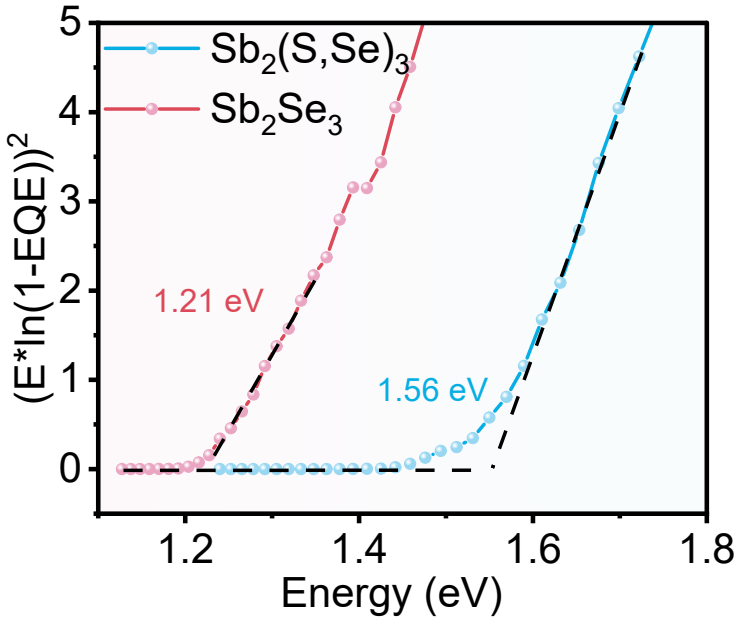

Fig. S32 Bandgap (Eg) of the subcells for 4-T TSCs cell.

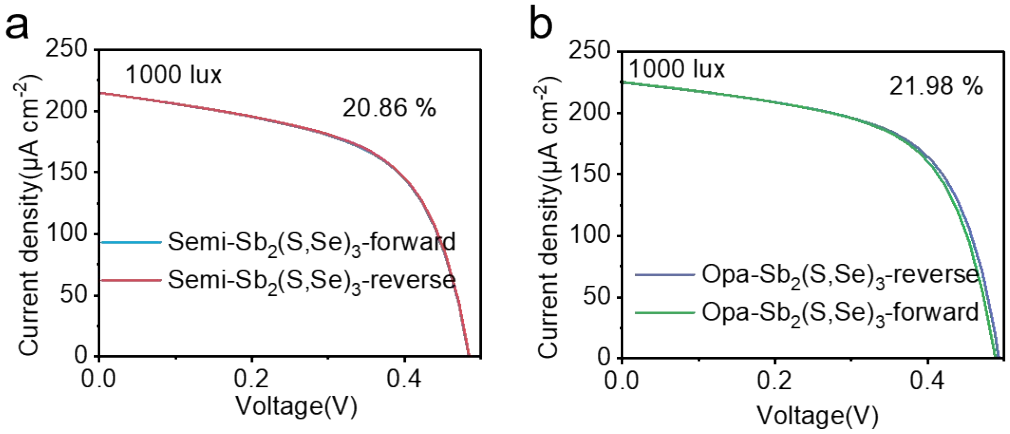

Fig. S33 J-V curves of the (a) ST-SSCs and (b) Opa-SSCs at the light intensity of 1000 lux under LED (3000 K).

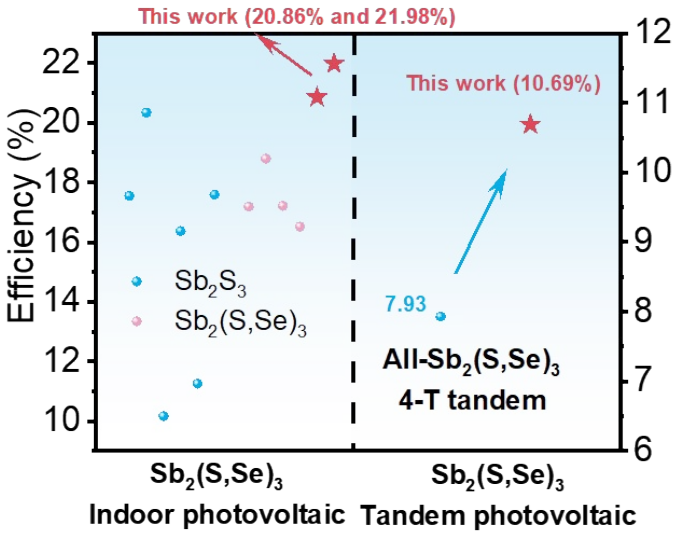

Fig. S34 The summarized PCEs of $Sb_2(S,Se)_3$ indoor photovoltaic performance and the all-$Sb_2(S,Se)_3$ tandem solar cells.

Table S1. Average transmittance in 400-1200 nm, visible region (400-800 nm), and NIR region (800–1200 nm) of IZO films.

Power density (W/cm^2)	400-800 nm (%)	800-1200 nm (%)	400-1200 nm (%)
1.42	79.56	82.77	81.16
3.54	80.72	78.80	79.76

Table S2. The optimal performance of the devices based on different power densities.

Power density (W/cm^2)	V_{OC} (V)	J_{SC} (mA/cm^2)	FF (%)	PCE (%)
0	0.535	20.33	54.74	5.95
1.06	0.624	20.18	61.24	7.71
1.42	0.647	20.04	63.71	8.26
1.95	0.643	20.22	61.75	8.03
2.78	0.635	20.35	58.05	7.50
3.54	0.593	20.15	57.15	6.83

Table S3. Device parameters of semitransparent $Sb_2(S,Se)_3$ Solar Cells with low power density sputtered ITO and IZO electrodes.

Devices	V_{OC} (V)	J_{SC} (mA/cm^2)	FF (%)	PCE (%)
Semi-ITO (1.42W/cm^2)	0.579	20.13	58.00	6.76
Semi-IZO	0.647	20.04	63.71	8.26

Table S4. Photovoltaic performance of the semitransparent $Sb_2(S,Se)_3$ solar cells with IZO alone and IZO+ITO electrodes.

Devices	V_{OC} (V)	J_{SC} (mA/cm^2)	FF (%)	PCE (%)
Semi-IZO-alone	0.646	20.21	60.35	7.89
Semi-IZO+ITO	0.647	20.04	63.71	8.26

Table S5. Parameters such as free carrier densities, bulk and interface defect densities, and depletion width obtained from DLCP and C-V characterization.

Samples	N_{cv}-N_{DLCP} (cm^{-3})	W_d (nm)	(N_{cv} – N_{DLCP}) x W_d (cm^{-2})
Semi-Control	$1.85x10^{17}$	97.8	$1.81x10^{12}$
Semi-IZO	$0.96x10^{17}$	143	$1.37x10^{12}$
Opa-Control	$7.36x10^{16}$	126	$0.93x10^{12}$
Opa-IZO	$7.85x10^{16}$	136	$1.07x10^{12}$

Table S6. The charge extraction characteristic for the complete semitransparent device from the Rear side.

Samples	A_1	τ_1 (ns)	A_2	τ_2 (ns)	τ_{ave} (ns)	k_{ht} ($10^7 s^{-1}$)
$Sb_2(S,Se)_3$	0.62	0.38	0.38	19.8	19.26	
$Sb_2(S,Se)_3$/MnS	0.71	0.26	0.29	15.8	15.19	1.38
$Sb_2(S,Se)_3$/MnS/ITO	0.71	0.16	0.29	8.81	8.43	6.66
$Sb_2(S,Se)_3$/MnS/IZO/ITO	0.77	0.051	0.23	6.09	5.92	11.68

Table S7. Charge extraction characteristic of the complete semitransparent device measured by incidence from the Front side of the device.

Samples	A_1	τ_1 (ns)	A_2	τ_2 (ns)	τ_{ave} (ns)
ITO-CdS/$Sb_2(S,Se)_3$	0.61	0.0545	0.39	5.94	5.86
IZO-CdS/$Sb_2(S,Se)_3$	0.52	0.0535	0.48	5.97	5.91

Table S8. Device parameters (average and champion) of solar cells based on Semi-control, Semi-IZO, Opa-control and Opa-IZO devices.

Devices	V_{OC} (V)	J_{SC} (mA/cm^2)	FF (%)	PCE (%)
Semi-CT	0.535 (0.531±0.013)	20.33 (20.09±0.53)	54.74 (47.80±6.34)	5.95 (5.10±0.68)
Semi-IZO	0.647 (0.648±0.007)	20.04 (20.08±0.27)	63.71 (62.58±1.56)	8.26 (8.14±0.12)
Opa-CT	0.647 (0.644±0.003)	21.53 (21.67±0.21)	64.15 (63.35±0.66)	8.94 (8.84±0.06)
Opa-IZO	0.649 (0.648±0.005)	21.51 (21.47±0.33)	69.46 (68.98±0.70)	9.70 (9.61±0.11)

Table S9. Summarized PCEs of related researches on semitransparent Sb-based solar cells.

Absorbers	V_{OC} (V)	FF (%)	J_{SC} (mA/cm^2)	PCE (%)	Ref.	Year
Sb_2S_3	0.612	46	13.8	3.9	[6]	2022
Sb_2S_3	0.58	41.72	8.76	2.13	[7]	2024
Sb_2S_3	0.560	49	6.12	1.67	[8]	2022
Sb_2S_3	0.679	41.96	12.07	3.44	[9]	2020
Sb_2S_3	0.68	53	13.7	4.94	[10]	2023
Sb_2S_3	0.664	52.42	16.03	5.58	[11]	2020
$Sb_2(S,Se)_3$	0.541	58.3	23.4	7.41	[12]	2023
$Sb_2(S,Se)_3$	0.647	63.71	20.04	8.26	This work	

Table S10. Summarized PCEs of the opaque all-inorganic $Sb_2(S,Se)_3$ solar cells.

HTLs	V_{OC} (V)	FF (%)	J_{SC} (mA/cm^2)	PCE (%)	Ref.	Year
$CsPbBr_3$	0.62	58.55	21.5	7.82	[13]	2020
MnS	0.664	65.48	21.26	9.24	[14]	2022
MnS	0.655	64.2	22.98	9.6	[4]	2022
MoS_2	0.76	59	13.9	6.1	[15]	2023
PbS	0.688	59.93	18.51	7.63	[16]	2023
MoO_3	0.683	63.75	16.53	7.20	[17]	2022
PbS	0.65	65.06	18.8	8.0	[18]	2022
Sb_2Se_3	0.647	64.86	18.49	7.75	[19]	2022
MXene	0.64	62.7	20.9	8.29	[20]	2021
Without	0.524	53.2	25.2	7.03	[21]	2021
Without	0.514	59.1	26.8	8.17	[22]	2021
Without	0.475	61.40	25.05	7.31	[23]	2021
Carbon	0.645	40.6	10.08	2.64	[24]	2018
PbS	0.51	53.69	20.05	5.46	[25]	2024
MnS	0.415	52.77	23.79	5.22	[5]	2024
NiOx	0.643	60.14	19.12	7.40	[26]	2024
SnS-NiOx	0.638	50.0	20.09	6.41	[27]	2024
Without	0.479	55.7	25.4	6.78	[28]	2023
Substrate	0.47	57.62	26.5	7.1	[29]	2023
Without	0.472	61.7	23.8	6.94	[30]	2023
Without	0.481	62.2	23.8	7.12	[31]	2023
Substrate	0.463	41.1	21.43	4.05	[32]	2022
Without	0.408	60.7	26.1	7.1	[33]	2022
Sb_2Se_3	0.43	61.71	28.22	7.49	[34]	2021
Carbon	0.74	55.8	12.5	5.2	[35]	2020
Without	0.46	54.2	29.6	7.27	[36]	2020
MnS/IZO	0.649	69.5	21.5	9.70	This work	

Table S11. The indoor photovoltaic performance of semitransparent and opaque solar cells.

Devices	V_{OC} (V)	J_{SC} (mA/cm^2)	FF (%)	PCE (%)
Semi-froward	0.485	215.8	57.14	20.75
Semi-reverse	0.485	214.8	57.42	20.86
Opa-froward	0.489	225.3	59.53	21.69
Opa-reverse	0.493	225.1	59.85	21.98

Table S12. photovoltaic performance of the $Sb_2(S,Se)_3$ semitransparent top subcell, Sb_2Se_3 bottom subcell, Sb_2Se_3 bottom subcell with a $Sb_2(S,Se)_3$ top cell filter and the 4-terminal tandem cell.

Devices	V_{OC} (V)	J_{SC} (mA/cm^2)	FF (%)	PCE (%)
$Sb_2(S,Se)_3$ top cell	0.655	20.13	62.30	8.22
Sb_2Se_3 solar cell	0.470	29.81	64.85	9.08
Filtered Sb_2Se_3 bottom cell	0.424	8.92	65.30	2.47
4T tandem cell				10.69

1. References

[1] W. Han, Q. Xu, J. Wang, J. Liu, Y. Li, Q. Huang, B. Shi, S. Xu, Y. Zhao, X. Zhang, *Prog Photovolt Res Appl*. 2023, **31**, 1032.

[2] R. Tang, X. Wang, W. Lian, J. Huang, Q. Wei, M. Huang, Y. Yin, C. Jiang, S. Yang, G. Xing, S. Chen, C. Zhu, X. Hao, M. A. Green, T. Chen, *Nat. Energy* 2020, **5**, 587.

[3] Xingyu Pan, Yanlin Pan, Lijun Wang, Chunhu Zhao, Xiaobo Hu, Jinchun Jiang, Bochuan Yang, Shaoqiang Chen, Pingxiong Yang, Junhao Chu, Jiahua Tao, *Ceramics International* 2023, **49**, 22471

[4] C. Qian, J. Li, K. Sun, C. Jiang, J. Huang, R. Tang, M. Green, B. Hoex, T. Chen, X. Hao, *J. Mater. Chem. A* 2022, **10**, 2835.

[5] J. Yang, H. Wang, B. Che, L. Huang, J. Gao, Z. Cai, C. Zhu, R. Tang, T. Chen, *Sol. RRL* 2024, **8**, 2400006.

[6] N. Juneja, S. Mandati, A. Katerski, N. Spalatu, S. Daskeviciute-Geguziene, A. Vembris, S. Karazhanov, V. Getautis, M. Krunks, I. O. Acik, *Sustain. Energy Fuels* 2022, **6**, 3220.

[7] P. Kumar, M. Eriksson, D. S. Kharytonau, S. You, M. M. Natile, A. Vomiero, *ACS Appl. Energy Mater.* 2024, **7**, 1421.

[8] P. Kumar, S. You, A. Vomiero, *J. Mater. Chem. C* 2022, **10**, 16273.

[9] S.-J. Lee, S.-J. Sung, K.-J. Yang, J.-K. Kang, J. Y. Kim, Y. S. Do, D.-H. Kim, *ACS Appl. Energy Mater.* 2020, **3**, 12644.

[10] S. Mandati, N. Juneja, A. Katerski, A. Jegorovė, R. Grzibovskis, A. Vembris, T. Dedova, N. Spalatu, A. Magomedov, S. Karazhanov, V. Getautis, M. Krunks, I. Oja Acik, *ACS Appl. Energy Mater.* 2023, **6**, 3822.

[11] J. Zhang, W. Lian, Y. Yin, X. Wang, R. Tang, C. Qian, X. Hao, C. Zhu, T. Chen, *Solar RRL* 2020, **4**, 2000048.

[12] C. Qian, K. Sun, J. Cong, H. Cai, J. Huang, C. Li, R. Cao, Z. Liu, M. Green, B. Hoex, T. Chen, X. Hao, *Adv. Mater* 2023, **35**, 2303936.

[13] C. Jiang, J. Yao, P. Huang, R. Tang, X. Wang, X. Lei, H. Zeng, S. Chang, H. Zhong, H. Yao, C. Zhu, T. Chen, *Cell Rep. Phys. Sci.* 2020, **1**, 100001.

[14] S. Wang, Y. Zhao, L. Yao, C. Li, J. Gong, G. Chen, J. Li, X. Xiao, *Sci. Bull.* 2022, **67**, 263.

[15] L. Lin, F. Wu, Z. Huang, L. Yao, H. Li, R. Liao, A. Chen, J. Li, G. Chen, *ACS Appl. Energy Mater.* 2023, **6**, 10415.

[16] P. Tang, Z.-H. Huang, Y.-X. Chen, H. Li, L.-Q. Yao, H. Li, L.-M. Lin, J.-R. Cai, Y.-L. Zhan, D. Wei, S.-Y. Chen, D.-Q. Chen, G.-L. Chen, *Chem. Eng. J.* 2023, **477**, 146722.

[17] Y. Xing, H. Guo, J. Liu, S. Zhang, J. Qiu, N. Yuan, J. Ding, *J. Alloys Compd.* 2022, **927**, 166842.

[18] F. Wu, Y. Zhao, L. Yao, H. Li, Z. Huang, L. Lin, Y. Ma, S. Chen, J. Li, G. Chen, *Chem. Eng. J.* 2022, **440**, 135872.

[19] G. Li, Y. Huang, R. Tang, B. Che, P. Xiao, W. Lian, C. Zhu, T. Chen, *Chinese Phys. B* 2022, **31**, 038803.

[20] H. Li, L. Lin, L. Yao, F. Wu, D. Wei, G. Liu, Z. Huang, S. Chen, J. Li, G. Chen, *Adv. Funct. Mater.* 2022, **32**, 2110335.

[21] Y. Lu, K. Li, X. Yang, S. Lu, S. Li, J. Zheng, L. Fu, C. Chen, J. Tang, *ACS Appl. Mater. Interfaces* 2021, **13**, 46858.

[22] Y. Pan, X. Hu, Y. Guo, X. Pan, F. Zhao, G. Weng, J. Tao, C. Zhao, J. Jiang, S. Chen, P. Yang, J. Chu, *Adv. Funct. Mater.* 2021, **31**, 2101476.

[23] X. Hu, J. Tao, R. Wang, Y. Wang, Y. Pan, G. Weng, X. Luo, S. Chen, Z. Zhu, J. Chu, H. Akiyama, *J. Power Sources* 2021, **493**, 229737.

[24] W. Wang, G. Chen, Z. Wang, K. Wang, S. Chen, Z. Huang, X. Wang, T. Chen, C. Zhu, X. Kong, *Electrochimica Acta* 2018, **290**, 457.

[25] H. Li, R. D, L. Yao, H. Li, P. Tang, J. Cai, L. Lin, S. Chen, D. Wei, G. Chen, *J. Alloys Compd.* 2024, **991**, 174492.

[26] S. Huang, Y. Xing, H. Zhu, T. Zhang, K. Geng, Y. Yang, H. Zhang, Q. Gu, J. Qiu, S. Jiang, H. Guo, N. Yuan, J. Ding, *J. Mater. Chem. C* 2024, **12**, 3098.

[27] J. Li, X. Hu, X. Zheng, Z. Gao, S. Wang, Y. Liu, C. Wang, W. Shao, G. Fang, *Energy Technol.* 2024, **12**, 2300694.

[28] D. Qin, X. Pan, R. Wang, Y. Pan, Y. Wang, J. Zhang, X. Ding, Y. Chen, S. Zheng, S. Ye, Y. Pan, G. Weng, X. Hu, J. Tao, Z. Zhu, J. Chu, H. Akiyama, S. Chen, *Sol. Energy Mater. Sol. Cells* 2023, **263**, 112582.

[29] Y.-C. Lin, C.-H. Chang, Y.-J. Hung, *Sol. Energy Mater. Sol. Cells* 2023, **259**, 112464.

[30] X. Pan, Y. Pan, L. Wang, C. Zhao, X. Hu, J. Jiang, B. Yang, S. Chen, P. Yang, J. Chu, J. Tao, *Ceram. Int.* 2023, **49**, 22471.

[31] X. Pan, Y. Pan, L. Shen, L. Wang, R. Wang, G. Weng, J. Jiang, X. Hu, S. Chen, P. Yang, J. Chu, J. Tao, *Adv. Funct. Mater.* 2023, **33**, 2214511.

[32] G.-J. Chen, R. Tang, S. Chen, Z.-H. Zheng, Z.-H. Su, H.-L. Ma, X.-H. Zhang, P. Fan, G.-

X. Liang, *ACS Appl. Mater. Interfaces* 2022, **14**, 31986.

[33] Y. Pan, X. Pan, R. Wang, X. Hu, S. Chen, J. Tao, P. Yang, J. Chu, *ACS Appl. Energy Mater.* 2022, **5**, 7240.

[34] S. Chen, M. Ishaq, W. Xiong, U. A. Shah, U. Farooq, J. Luo, Z. Zheng, Z. Su, P. Fan, X. Zhang, G. Liang, *Sol. RRL* 2021, **5**, 2100419.

[35] L. Yao, L. Lin, H. Liu, F. Wu, J. Li, S. Chen, Z. Huang, G. Chen, *J. Mater. Sci. Technol.* 2020, **58**, 130.

[36] K. Li, Y. Lu, X. Ke, S. Li, S. Lu, C. Wang, S. Wang, C. Chen, J. Tang, *Sol. RRL* 2020, **4**, 2000220.